High-Temperature Materials

SCIEPublish

Article

Preparation of $MgAl_2O_4$ Porous Ceramics for High-Temperature Flue Gas Filtration Application by *In-Situ* Decomposition Method

Jiarong Li [1], Lei Zhang [2], Xiaojie Ji [1], Chenran Zhang [1], Jianbiao Kong [2], Zheng Zhang [1,3], Wenying Zhou [1,*] and Degang Zhao [1,*]

[1] School of Materials Science and Engineering, University of Jinan, Jinan 250022, China; lijr1@stu.ujn.edu.cn (J.L.); stu_jxj@stu.ujn.edu.cn (X.J.); zhangcr@stu.ujn.edu.cn (C.Z.); mse_zhangz@ujn.edu.cn (Z.Z.)

[2] Heze Institute of Product Inspection and Testing, Heze 274000, China; sdhzzl@sohu.com (L.Z.); sdhzjcy@sohu.com (J.K.)

[3] CNRS, CEMHTI UPR3079, University of Orléans, 45000 Orléans, France

* Corresponding author. E-mail: mse_zhouwy@ujn.edu.cn (W.Z.); mse_zhaodg@ujn.edu.cn (D.Z.)

Received: 29 January 2026; Revised: 24 February 2026; Accepted: 13 March 2026; Available online: 23 March 2026

ABSTRACT: Porous ceramic filters exhibit excellent prospects for application in the field of high-temperature flue gas filtration. In this study, the $MgAl_2O_4$ porous ceramics were prepared using α-Al_2O_3, MgO, and EDTA-$MgNa_2$ as raw materials by the *in-situ* decomposition method. The effect of the introduction of EDTA-$MgNa_2$ on phase composition and microstructure, as well as the correlation between the content of EDTA-$MgNa_2$ and ceramic properties, was investigated using XRD, SEM, and EDS. The results revealed that the introduction of EDTA-$MgNa_2$ formed pores, thereby improving gas permeability. Additionally, the addition of EDTA-$MgNa_2$ was beneficial for the formation of a transitional liquid and promoted sintering, thereby slowing the decrease in compressive strength. The optimal specimen is the ceramic with 10 wt% EDTA-$MgNa_2$, which exhibits a high porosity of 56.28%, a compressive strength of 10.93 MPa, and a high gas permeability coefficient (8.84×10^{-9} m^2).

Keywords: $MgAl_2O_4$; Porous ceramics; *In-situ* decomposition; Flue gas filtration

1. Introduction

Although energy sources such as wind and solar power have developed rapidly, fossil fuels still remain the main source of energy generation. However, their combustion emits large amounts of high-temperature flue gases [1,2] containing acid corrosive gases (CO, CO_2, SO_2) [3] and dust particles (PM), which can destroy the ecological environment [4–6]. To reduce such environmental pollution, porous ceramics are used as filters to filter the flue gas before emission. Generally, SiC porous ceramics with their exceptional thermal stability [7] and substantial specific surface area are suitable for filtering flue. However, high-temperature flue gas can erode SiC ceramics, thereby reducing their service life. Furthermore, the susceptibility of SiC ceramics to oxidation limits their operating temperature and makes them prone to failure. Hence, it is worth investigating alternative materials to produce advanced porous ceramics with excellent inoxidizability, greater chemical stability, and improved filtration performance. Compared with

SiC, $MgAl_2O_4$ offers high melting point, high temperature stability, and good corrosion resistance, making it a promising candidate for high-temperature filtration applications [2,8–10].

Gas permeability is one of the most important properties of porous ceramic filters and is affected by porosity, pore size, and pore connectivity [11]. To introduce pores into the ceramic, the pore-forming agent method, gel-casting method, and freeze-drying [12] have been applied. Kumar et al. [11] prepared Al_2O_3 based ceramic filters by adding a pore-forming agent method with characteristics of an apparent porosity of 39–70%, a compressive strength of 6–82 MPa, and a relatively high gas permeability coefficient of 0.38 × 10^{-10}–9.15 × 10^{-10} m^2. Liu et al. [13] use gel-casting method and freeze-drying method to prepare the mullite porous ceramics with a high apparent porosity of 56.04–75.34%, a compressive strength of 0.61–3.03 MPa, and a gas permeability coefficient of 1.11 × 10^{-10}–4.73 × 10^{-11} m^2. Based on the above analysis, various porous ceramics with a high apparent porosity have been fabricated by these methods. However, the high porosity results in a low compressive strength. Compared with the above method, the *in-situ* decomposition method, which relies on the decomposition of raw materials, offers a more uniform pore size distribution, thereby helping to preserve the compressive strength of porous ceramic filters. For instance, Zhou et al. [14] prepared $MgAl_2O_4$ porous ceramics via the decomposition of bauxite and magnesite, with characteristics of a density of 3.43 g/cm^3 and a flexural strength of 93.5 MPa. Wang et al. [15] prepared $MgAl_2O_4$ porous ceramics by the *in-situ* decomposition method, achieving an optimal sample with an apparent porosity of 50%, a flexural strength of 35.06 MPa, and a nitrogen gas flux of 3057 $m^3 \cdot m^{-2} \cdot h^{-1}$ under the gas pressure of 0.1 MPa. It can therefore be concluded that the *in-situ* decomposition method is an effective method for improving the strengths of $MgAl_2O_4$ porous ceramic.

EDTA-$MgNa_2$ is an organic magnesium compound that decomposes to generate more gas during sintering. When used for the *in-situ* decomposition, it provides a new opportunity to enhance the pore interconnectivity between pores. During the sintering process, EDTA-$MgNa_2$ also releases Na^+ ions that react with impurity ions in the raw materials to form a transitional liquid phase, thereby promoting the sintering reaction. Combined with the *in-situ* decomposition method, this approach enables the formation of uniformly sized pores, ultimately optimizing the balance between compressive strength and gas permeability. Based on the above analysis, preparing porous ceramics via the *in-situ* decomposition method using EDTA-$MgNa_2$ as a raw material is expected to yield high-temperature porous $MgAl_2O_4$ ceramic with high compressive strength and high gas permeability.

In this study, a $MgAl_2O_4$ porous ceramic filter was prepared via the *in-situ* decomposition method, using α-Al_2O_3, MgO, and EDTA-$MgNa_2$ as raw materials. The influence of EDTA-$MgNa_2$ content on the phase composition, microstructure, apparent porosity, pore size distribution, thermal expansion coefficient, mechanical properties, and gas permeability of $MgAl_2O_4$ porous ceramics was investigated to verify the feasibility of $MgAl_2O_4$ as a high-temperature flue gas filter.

2. Materials and Methods

2.1. Raw Materials

α-Al_2O_3 (purity ≥ 99.99%, D_{50} = 4.00 μm, Shandong Higiant High-Purity Alumina Technology Co., Ltd., Binzhou, China), MgO (purity ≥ 99.90%, D_{50} = 5.00 μm, Hebei Zhuyan Alloy Materials Co., Ltd., Xingtai, China), and EDTA-$MgNa_2$ (Shandong Smatts Agricultural Science and Technology Co., Ltd., Weifang, China) were used as the main material. C_2H_5OH (Tianjin Fuyu Chemical Co., Ltd., Tianjin, China) was chosen as a binder.

2.2. Specimen Preparation

In order to form stoichiometric $MgAl_2O_4$ spinel, the weight ratio of Al_2O_3 and MgO was chosen as 2.53:1. Firstly, the raw materials were mixed with ethyl alcohol using a mortar and pestle for 5 min

according to the designed compositions described in Table 1. EDTA-$MgNa_2$ with the contents of 0.0 wt%, 2.5 wt%, 5.0 wt%, 7.5 wt%, or 10.0 wt% was introduced, and the samples were named as M1, M2, M3, M4, M5. Dry mixtures were pressed uniaxially in a hydraulic press at 20 MPa to φ30 × H10 mm and φ20 × H20 mm. The green samples were then dried in an oven at 110 °C for 24 h. Finally, the samples were placed in a muffle furnace with an air atmosphere and sintered at a heating rate of 5 °C/min. During the sintering process, they were pre-fired at 700 °C for 3 h, then sintered at 1500 °C for 3 h, and allowed to cool down to room temperature at a rate of 5 °C/min inside the furnace.

Table 1. Sample codes with different compositions.

Sample Codes	Al_2O_3 (wt%)	MgO (wt%)	EDTA-$MgNa_2$ (wt%)
M1	71.7	28.3	0.0
M2	70.1	27.4	2.5
M3	68.5	26.5	5.0
M4	66.9	25.6	7.5
M5	65.4	24.6	10.0

2.3. Characterizations

Thermal analysis of the EDTA-$MgNa_2$ was detected using a simultaneous TG-DSC apparatus (STA449, NETZSCH, Selb, Germany). The phase compositions of samples were determined via X-ray diffraction (Rigaku Smart Lab 9kW, Rigaku, Tokyo, Japan) with Cu Kα radiation in the 2θ range of 5–90° and a scanning speed of 2°/min. The microstructure was studied by field emission scanning electron microscopy (QUANTA 250 FEG, FEI Company, Hillsboro, OR, USA). The pore size distribution was examined via mercury porosimetry (AutoPore V 9600, Micromeritics, Norcross, GA, USA). The bulk density and apparent porosity were determined by the Archimedes method using water as the medium.

The linear change of the sample before and after calcination was determined by the following equation:

$$\text{Linear change} = \frac{l_2 - l_1}{l_1} \times 100\% \quad (1)$$

where l_1 and l_2 are the diameters of the samples before and after sintering.

The weight change of the sample before and after calcination was determined by the following equation:

$$\text{Weight change} = \frac{m_1 - m_2}{m_1} \times 100\% \quad (2)$$

where m_1 and m_2 are the weights of the samples before and after sintering.

The compressive strength was assessed using a universal testing machine (CMT5305, MTS Systems (China) Co., Ltd., Shanghai, China). The sample was cylindrical with 20 mm in diameter and 20 mm in height. Thermal expansion analysis was carried out in a thermomechanical analyzer (TMAPT1000, LINSEIS, Selb, Germany) from room temperature to 600 °C. The theoretical liquid phases were calculated by the Equilib mode of the thermo-chemical software Factsage 6.2.

As shown in Figure 1, a self-made pressure drop tester was used to measure the pressure drop of a gas across the ceramics. The device pipe's inner diameter and the test samples' diameter were 30 mm each. The tests were carried out at the gas velocity of 10–19 m/s. According to previous research [16–19], the gas permeability coefficient and the ceramic permeance were calculated by using Equations (3) and (4):

$$\psi = \frac{\eta Q t}{A \Delta P} \quad (3)$$

where ψ is the permeability coefficient (m^2), η is the dynamic viscosity of air, Q is the gas flow rate (m^3/s), t is the thickness of the sample (m), A is the filter area (m^2), and ΔP is the pressure drop (Pa).

$$\text{Permeance} = \frac{\text{Flux}}{\Delta PA} = \frac{n}{\Delta PA} \quad (4)$$

The term "permeance" refers to gas permeance ($mol \cdot m^{-2} \cdot s^{-1} \cdot Pa^{-1}$), while n is the flow rate of the gas ($mol \cdot s^{-1}$).

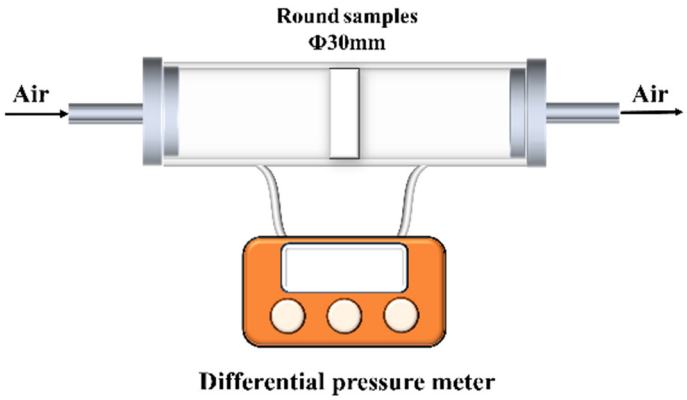

Figure 1. Schematic diagram of the test device for gas filtration pressure drop.

3. Results and Discussion

3.1. Thermal Stability of EDTA-MgNa2

In order to determine the heat treatment process, the dehydration and thermal stability of EDTA-$MgNa_2$ were investigated through the TG-DSC analysis, as depicted in Figure 2. The DSC curve can be divided into three stages. In the first stage, with the temperatures ranging from ambient to 186.27 °C, the mass of specimens was reduced to 79%, due to the vaporization of the physisorbed water. In the second stage, when the temperature increased to 624.17 °C, EDTA-$MgNa_2$ decomposed, releasing gases such as CO and CO_2 [20], and formed $MgCO_3$ and Na_2CO_3, as shown in Equation (5).

$$C_{10}H_{12}MgN_2Na_2O_8(s) = MgCO_3(s) + Na_2CO_3(s) + CO_2(g) + H_2O(g) + NO_x(g) \quad (5)$$

Further increasing the temperature to 667.67 °C, $MgCO_3$ decomposed into MgO and CO_2, as depicted in Equation (6).

$$MgCO_3(s) = MgO(s) + CO_2(g) \quad (6)$$

Upon further heating to 700 °C, the mass of MgO (the decomposition products of EDTA-$MgNa_2$) remained stable, with a mass residual rate of 15%. Therefore, since the decomposition of EDTA-$MgNa_2$ is completed at 700 °C, a holding step was chosen to be carried out at this temperature to ensure complete decomposition of EDTA-$MgNa_2$.

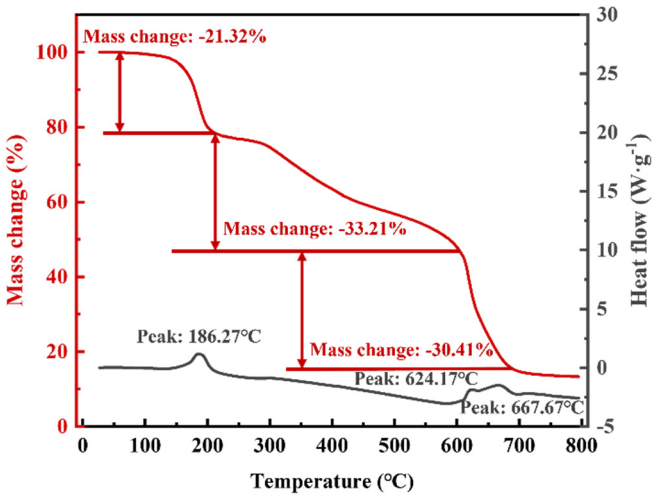

Figure 2. TG-DSC curve of the EDTA-$MgNa_2$.

3.2. Phase Compositions, Microstructures, and Pore Size Distributions of $MgAl_2O_4$ Ceramics

Figure 3 shows the XRD pattern of $MgAl_2O_4$ samples with different EDTA-$MgNa_2$ contents, indicating that the main phase of these ceramics was $MgAl_2O_4$. It is well established that Al_2O_3 and MgO can react in situ to form $MgAl_2O_4$ (Equation (7)). In this study, MgO originates from two sources: the MgO present in the raw materials and the MgO derived from the decomposition of EDTA-$MgNa_2$ (Figure 2). During the sintering process, both types of MgO can react with the Al_2O_3 in the raw materials to form $MgAl_2O_4$.

$$MgO(s) + Al_2O_3(s) = MgAl_2O_4(s) \quad (7)$$

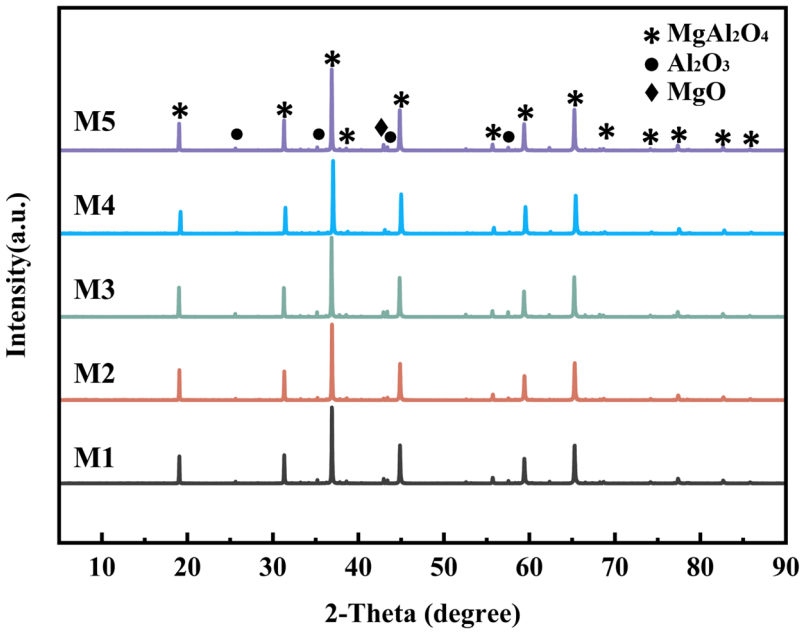

Figure 3. XRD pattern of the $MgAl_2O_4$ porous ceramics fired at 1500 °C with different EDTA-$MgNa_2$ contents.

Figure 4 shows the micromorphology of fired samples M1–M5 with different EDTA-$MgNa_2$ contents. Combined with EDS, the irregular particles are confirmed as $MgAl_2O_4$ grains, consistent with the XRD results shown in Figure 3. As shown in Figure 4a1–e1, the grain growth mechanism of $MgAl_2O_4$ can be described as follows: Initially, Al_2O_3 and MgO react to form $MgAl_2O_4$. As the reaction proceeds, more $MgAl_2O_4$ grains are formed and accumulated, resulting in larger grains until they reach the critical size.

Since the MgO derived from the decomposition of EDTA-$MgNa_2$ has higher reactivity, increasing the EDTA-$MgNa_2$ content leads to a greater number of fine grains.

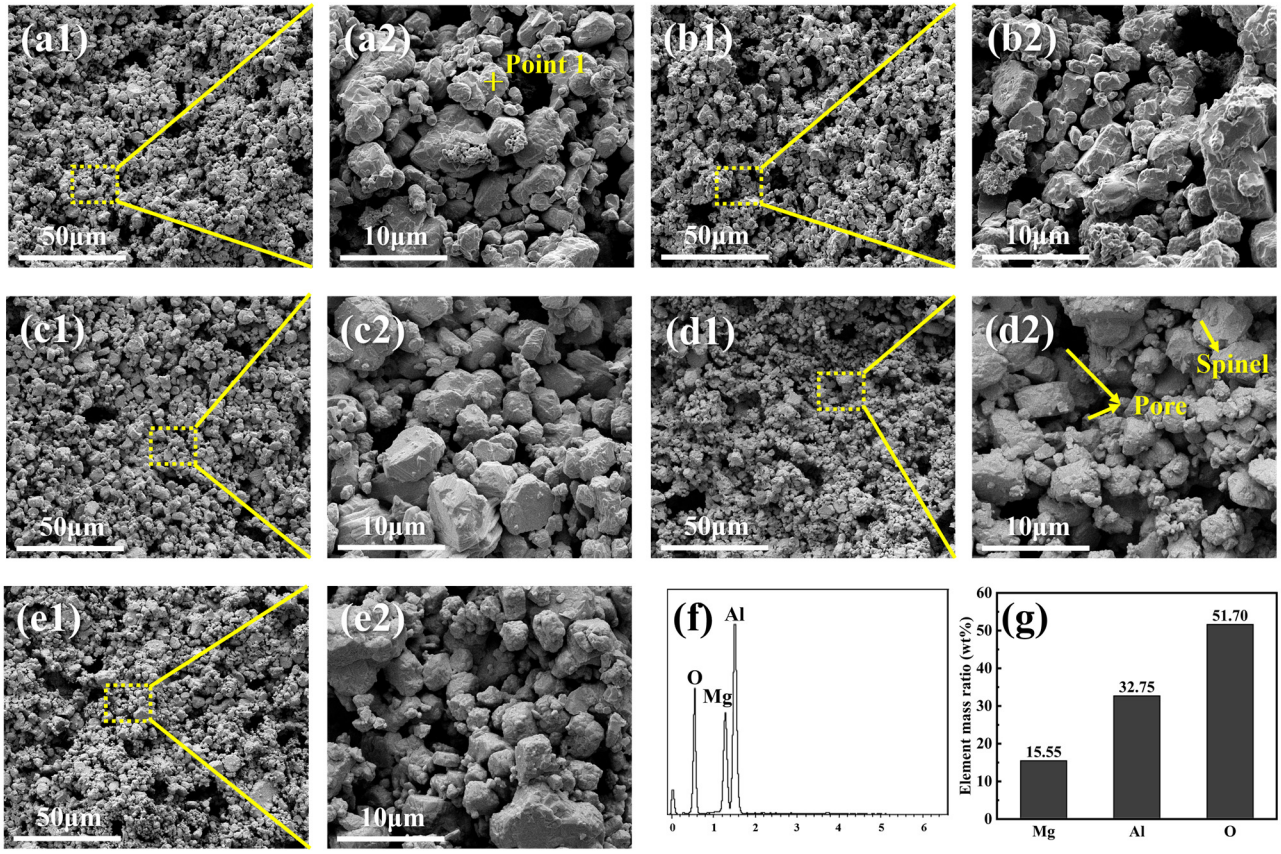

Figure 4. SEM images of the $MgAl_2O_4$ porous ceramics after firing at 1500 °C with different EDTA-$MgNa_2$ contents: (**a**) M1, (**b**) M2, (**c**) M3, (**d**) M4, (**e**) M5; EDS elemental analysis of point 1 in (**a2**): (**f**,**g**).

The SEM images of polished sample M5 sintered at 1500 °C are given in Figure 5. As shown in Figure 5a, the matrix is mainly $MgAl_2O_4$, with a large number of uniformly distributed pores. Additionally, a few regions exhibiting a multi-particle packing structure surrounded by $MgAl_2O_4$ and annular pores (Figure 5b) are observed. By combining Figure 5d–g, it reveals that this region with multi-particle packing structure corresponds to partially reacted MgO, and there are pores formed by the decomposition of EDTA-$MgNa_2$ between the MgO particles.

The pore structure parameters of $MgAl_2O_4$ porous ceramics are depicted in Figure 6. Analysis of Figure 6a reveals a unimodal distribution of the pore size in the porous ceramics with different EDTA-$MgNa_2$ contents, indicating that the pore size of the samples is uniformly distributed. As shown in Figure 6a, with the EDTA-$MgNa_2$ content increasing from 0 to 10 wt%, the pore size of $MgAl_2O_4$ porous ceramics shows an overall upward trend. The prominent peak value of the M5 sample reaches 4.09 μm, and a large pore size is conducive to enhancing the gas permeability of $MgAl_2O_4$ porous ceramics. As illustrated in Figure 6b, higher EDTA-$MgNa_2$ content resulted in an upward shift in the cumulative pore volume curve, indicating that samples containing higher EDTA-$MgNa_2$ content have better pore structure. The steep curve in the range of 0.70–7.20 μm reflects a rapid increase in cumulative pore volume, indicating that most pores fall within this size range, and a large and uniform pore size distribution is conducive to gas passing and flue gas filtration.

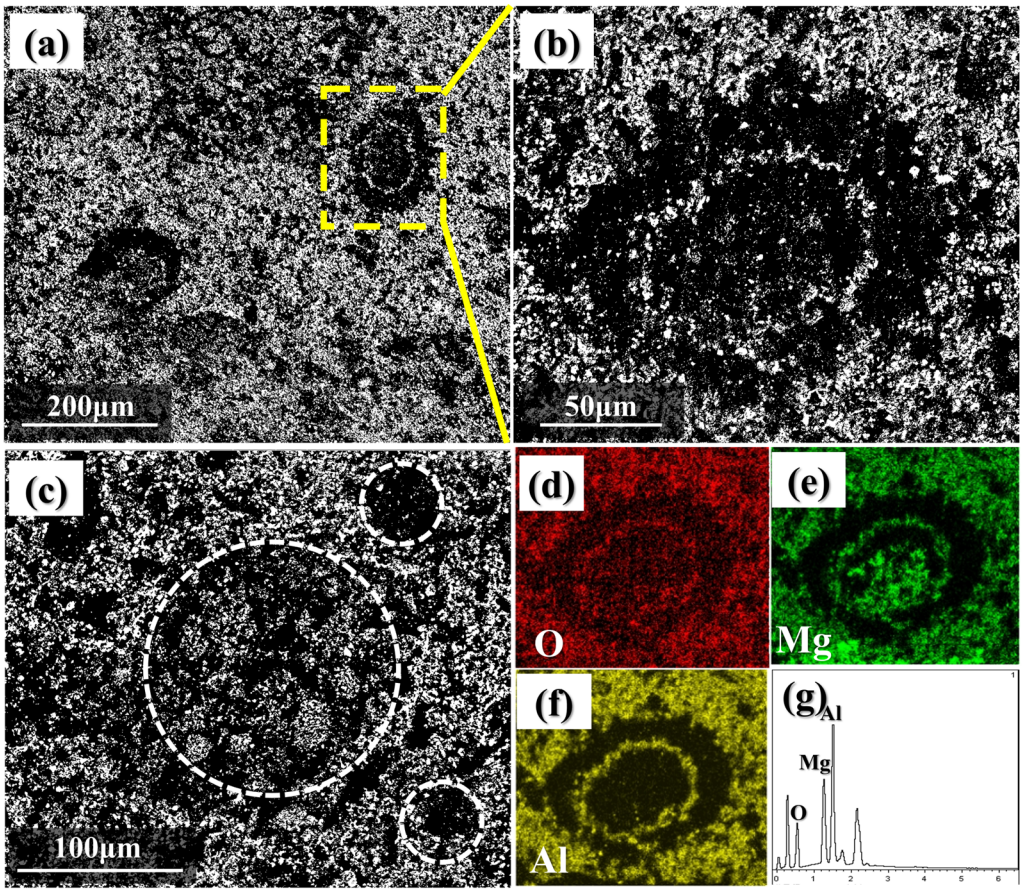

Figure 5. Microstructure of a polished sample M5 after firing at 1500 °C (**a**–**c**) SEM images; (**d**–**g**) element mapping analysis corresponding to O, Mg, and Al elements.

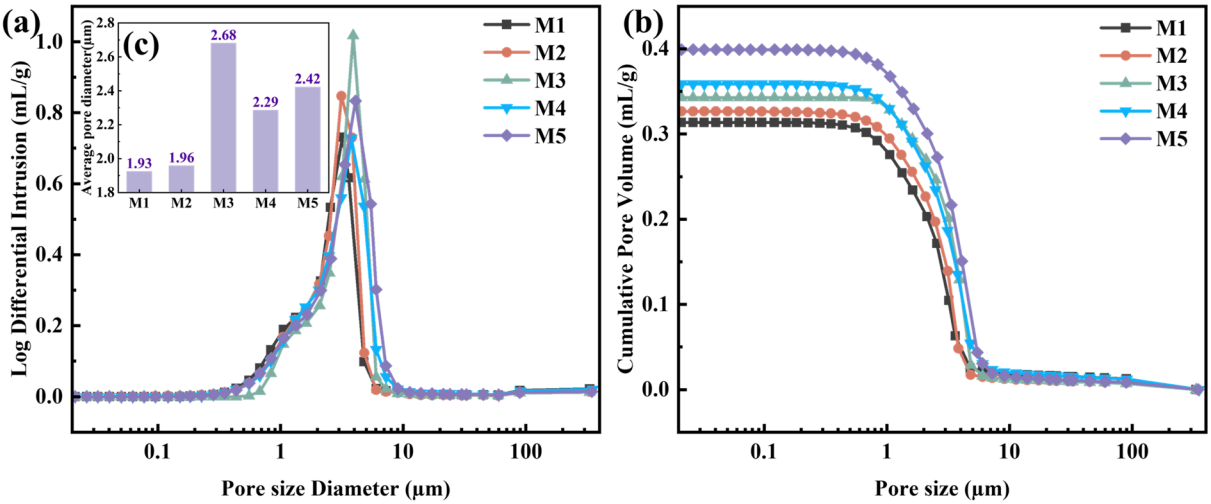

Figure 6. (**a**,**b**) Pore structure parameters and (**c**) average pore size of the $MgAl_2O_4$ porous ceramics after firing at 1500 °C with different EDTA-$MgNa_2$ contents.

Figure 7 shows the weight change and linear change of the $MgAl_2O_4$ porous ceramics with different EDTA-$MgNa_2$ contents. As shown in Figure 7, with the increase in EDTA-$MgNa_2$ content from 0.0 to 10.0 wt%, the weight change gradually increased from 1.32% to 10.57%, due to the decomposition of EDTA-$MgNa_2$ and release of gas [20]. The linear change of $MgAl_2O_4$ porous ceramics indicates that all samples exhibit thermal expansion characteristics, mainly due to the formation of spinel, which is accompanied by volume expansion [15,21].

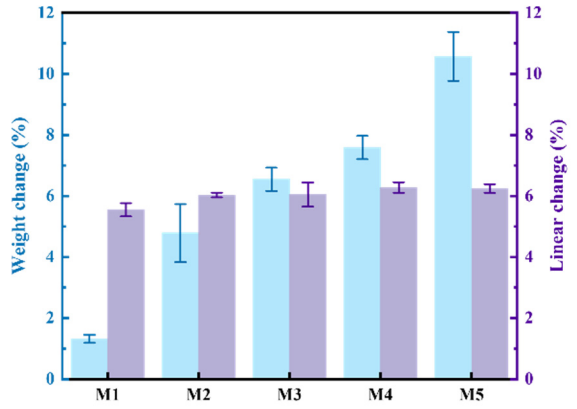

Figure 7. Weight change and linear change of the $MgAl_2O_4$ porous ceramics after firing at 1500 °C with different EDTA-$MgNa_2$ contents.

3.3. Physical Properties

Figure 8 illustrates the apparent porosity and bulk density of $MgAl_2O_4$ porous ceramics with different EDTA-$MgNa_2$ contents. The results showed that the apparent porosity of $MgAl_2O_4$ porous ceramics showed an upward trend from 47.27% to 56.28%, and the bulk density showed a down trend from 1.72 $g \cdot cm^{-3}$ to 1.45 $g \cdot cm^{-3}$ with increasing EDTA-$MgNa_2$ content. Then, by combining the apparent porosity with the linear change in Figure 6, it can be found that the $MgAl_2O_4$ spinel formation is beneficial for the apparent porosity due to the volume expansion. And as mentioned above, the EDTA-$MgNa_2$ is evenly distributed between the particles. After sintering, a large number of pores formed due to the decomposition of EDTA-$MgNa_2$. Thus, the $MgAl_2O_4$ porous ceramics prepared by this *in-situ* decomposition method exhibited high porosity, an important condition for achieving high gas permeability.

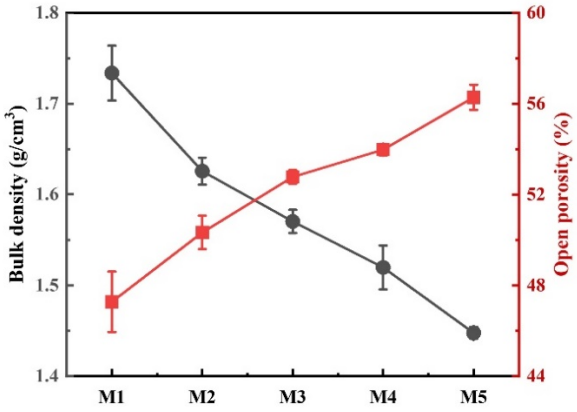

Figure 8. Apparent porosity and bulk density of the $MgAl_2O_4$ porous ceramics after firing at 1500 °C with different EDTA-$MgNa_2$ contents.

Figure 9 displays the compressive strength of $MgAl_2O_4$ porous ceramics with different EDTA-$MgNa_2$ contents. As observed, the compressive strength of $MgAl_2O_4$ porous ceramic decreased gradually from 35.56 to 10.93 MPa with increasing EDTA-$MgNa_2$ content. Compressive strength is a crucial index of material mechanical properties, while porosity is a key factor that is usually negatively correlated with material strength. The relationship between the two parameters can be described by the Gibson-Ashby model, as expressed by Equation (8) [19,22,23]:

$$\sigma \propto \sigma_s (1 - P)^m \quad (8)$$

where σ and σ_s represent the compressive strength of porous and dense material, respectively, P represents the porosity, and m is a constant.

As shown in Figure 8 and Equation (8), the compressive strength is negatively correlated with porosity (Figure 9b), indicating that higher apparent porosity reduces the load-bearing area of the material, thereby decreasing the compressive strength (Figure 9a). Thus, the porosity of the $MgAl_2O_4$ porous ceramics increased, and the strength decreased. However, the $MgAl_2O_4$ porous ceramics produced by the *in-situ* decomposition method still possess sufficient compressive strength to enable their industrial applications for high-temperature gas filtration.

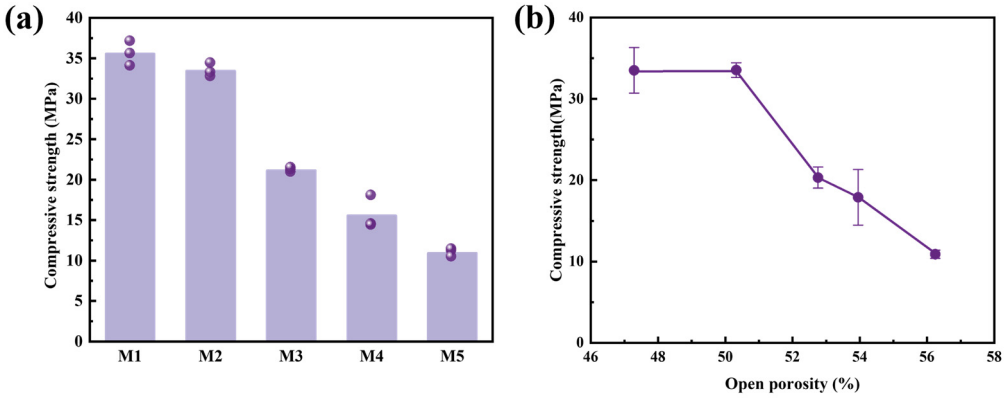

Figure 9. (**a**) Compressive strength; (**b**) linear relationship between compressive strength and apparent porosity of the $MgAl_2O_4$ porous ceramics after firing at 1500 °C with different EDTA-$MgNa_2$ contents.

Figure 10 presents the coefficients of thermal expansion (CTE) of $MgAl_2O_4$ porous ceramics prepared with varying EDTA-$MgNa_2$ contents. It is evident from the figure that the CTE of the $MgAl_2O_4$ porous ceramic increased gradually with the increasing test temperature, due to the average distance between atoms in the lattice increasing with the increase of temperature [24,25]. At 600 °C, as the content of EDTA-$MgNa_2$ increases from 0.0 to 2.5 wt% and from 5.0 to 7.5 wt%, the CTE values of the $MgAl_2O_4$ porous ceramic increase. This is because $MgAl_2O_4$ itself expands during heating. Although pores in the sample can absorb the displacement of some solid particles caused by heating, the poor connectivity of the pores limits their ability to improve the CTE. As the content of EDTA-$MgNa_2$ increases from 2.5 to 5.0 wt% and from 7.5 to 10.0 wt%, the CTE values of the $MgAl_2O_4$ porous ceramics decrease. This is attributed to the greater number of pores in the sample, which absorb the displacements of some solid particles caused by heating, thereby reducing the CTE. As a result, the $MgAl_2O_4$ porous ceramic with 10.0 wt% EDTA-$MgNa_2$ shows the lowest CTE of 7.93×10^{-6}/K.

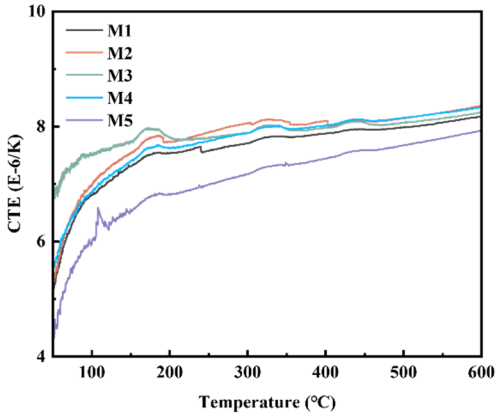

Figure 10. Coefficients of thermal expansion (CTE) of the $MgAl_2O_4$ porous ceramics after firing at 1500 °C with different EDTA-$MgNa_2$ contents.

3.4. Gas Permeability

Pressure drop is an important parameter to characterize the gas permeance of ceramic filters, which is caused by the energy loss of gas flow in the pipeline. Figure 11a shows the relationship between EDTA-$MgNa_2$ content and the pressure drop at flow velocities of 10–19 m/s. As shown in Figure 11a, the results indicate that the pressure drop gradually increased with increasing gas velocity, because resistance is generated as gas molecules collide with each other due to internal friction as they flow through a pipeline [26]. This resistance reduces the gas velocity, thereby increasing resistance to gas flow and leading to a rise in the pressure drop. However, as the gas velocity increases, the pressure drop of the M5 sample generally remains at a lower value, which is conducive to enhancing the gas permeability of $MgAl_2O_4$ porous ceramic in practical applications. As gas velocity increased to 19 m/s, the pressure drop of $MgAl_2O_4$ porous ceramic first increased and then decreased. The reason why the M2 sample has a higher pressure drop than the M1 sample is attributed to the presence of isolated small pores in the M2 sample, which will lead to longer and more tortuous paths in the sample when gas flows through. Subsequently, the number of interconnected pores in $MgAl_2O_4$ porous ceramic gradually improves, leading to a decreasing trend in pressure drop. Ultimately, the M5 sample achieved the minimum pressure drop of 3.39 hPa.

Figure 11b shows the gas permeability coefficient and gas permeance values of the $MgAl_2O_4$ porous ceramics with different EDTA-$MgNa_2$ contents at a gas flow velocity of 19 m/s. It can be observed that, as fundamental performance parameters of filter materials, the gas permeability coefficient and gas permeance indicate that all $MgAl_2O_4$ porous ceramics exhibit good gas permeability, consistent with the gas permeability coefficient reported in the literature [27]. Among them, the M5 sample had the maximum gas permeability coefficient and gas permeance of 8.84×10^{-9} m^2 and 1.52 $mol \cdot m^{-2} \cdot s^{-1} \cdot Pa^{-1}$, respectively, consistent with the phenomenon that the pressure drop decreases to 3.39 hPa. In summary, the content of EDTA-$MgNa_2$ can improve the gas permeability while maintaining the high filtration precision of $MgAl_2O_4$ porous ceramics, and the M5 sample is the optimal one.

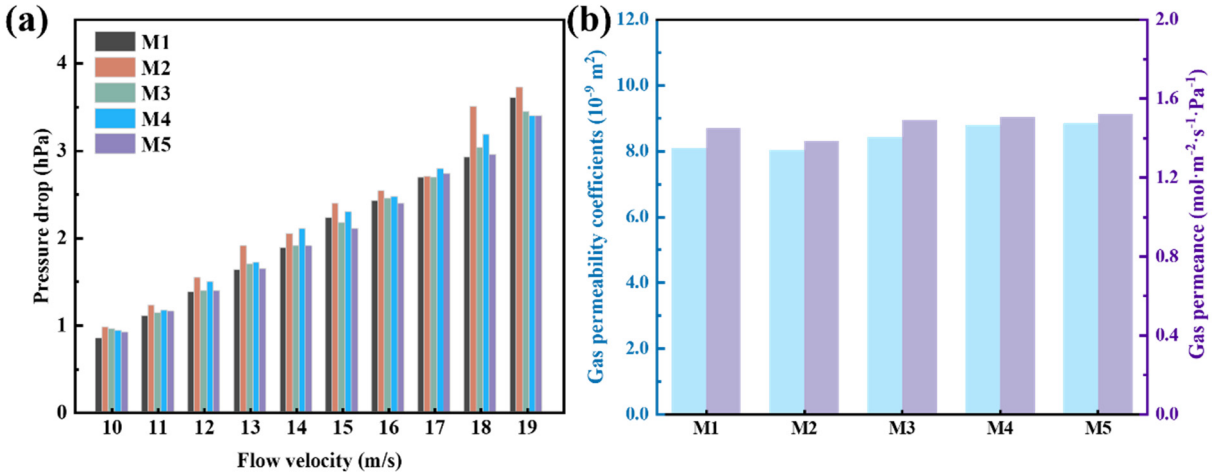

Figure 11. (**a**) Pressure drop at gas velocities of 10 m/s to 19 m/s; (**b**) gas permeability coefficient and gas permeance at a gas velocity of 19 m/s for $MgAl_2O_4$ porous ceramics after firing at 1500 °C with different EDTA-$MgNa_2$ contents.

4. Discussion

The above results indicate that the $MgAl_2O_4$ porous ceramics with high gas permeability are successfully prepared using MgO, Al_2O_3, and EDTA-$MgNa_2$ as raw materials through the *in-situ* decomposition method. The process will be discussed in three stages, as illustrated in Figure 12, focusing on EDTA-$MgNa_2$ decomposition, spinel formation, and pore structure.

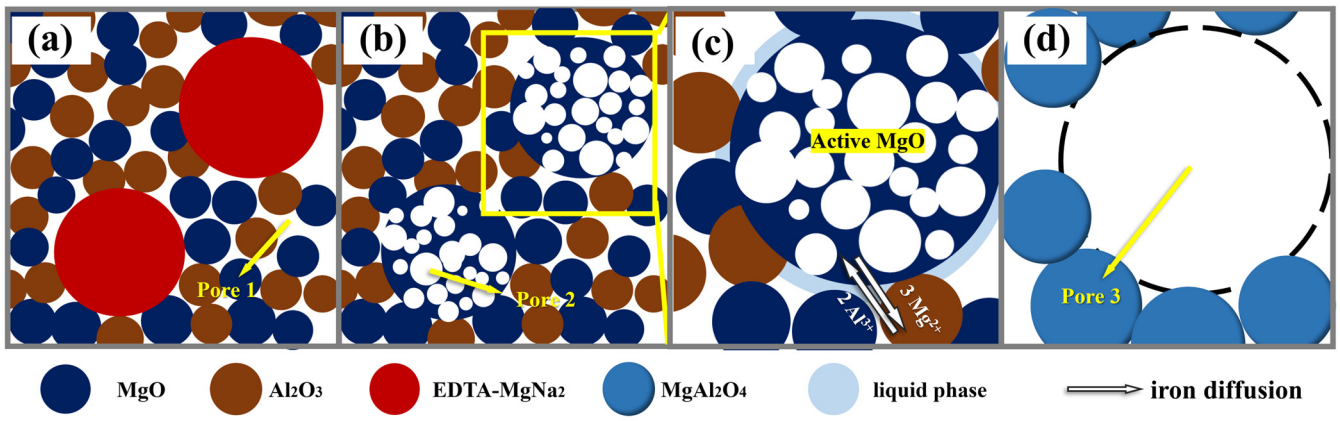

Figure 12. Schematic diagram of the sintering mechanism of $MgAl_2O_4$ porous ceramics: (**a**) initial process; (**b**) decomposition process; (**c**,**d**) sintering process.

(a) Initial Stage: As shown in Figure 12a, the green body primarily consists of large MgO and Al_2O_3 particles, and smaller EDTA-$MgNa_2$ particles. Pores (Pore 1) are observed in the green body, arising from particle packing during the dry pressing process.

(b) Decomposition Stage: During the heating process, the organic backbone of EDTA-$MgNa_2$ decomposes, and the C, H, and N elements react with oxygen to generate gases such as CO and CO_2, which are subsequently released. When the temperature reaches about 700 °C, EDTA-$MgNa_2$ particles completely decompose and form MgO grains with numerous pores (Pore 2), which may be the main reason for the significant increase in apparent porosity as the content of EDTA-$MgNa_2$ increases (Figure 8). As shown in Figure 12b, the presence of pores isolates most particles from one another (Figure 5b), thereby providing more interfacial area that serves as nucleation sites.

(c,d) Sintering Stage: As the sintering temperature increases, the liquid phase forms on MgO particles due to the presence of impurities in the raw materials and the Na^+ released from the EDTA-$MgNa_2$ decomposition. The effects of temperature and EDTA-$MgNa_2$ content on the liquid phase content of samples are shown in Figure 13. As can be seen, the liquid phase content increases gradually with higher EDTA-$MgNa_2$ content, reaching 2.85 wt% at 1500 °C when the EDTA-$MgNa_2$ content is 10 wt%. This increase in liquid phase accelerates the mutual diffusion of Mg^{2+} and Al^{3+}, thereby promoting the formation and deposition of $MgAl_2O_4$ spinel.

To achieve the electric neutrality during the formation of spinel, 2-mol Al^{3+} diffuses into the MgO side to produce 1 mol $MgAl_2O_4$, whereas 3-mol Mg^{2+} diffuses into the Al_2O_3 side [28,29]. As shown in Figure 5a,b, the presence of $MgAl_2O_4$ rims around those pores indicates that they were previously occupied by MgO particles, which led to a quicker formation of $MgAl_2O_4$ on the Al_2O_3 side, thereby triggering the Kirkendall effect and creating Kirkendall voids (Pore 3 and Figure 5c) [29,30]. Due to the different rate of ion diffusion, neck bonds will appear between particles, leading to agglomeration (Figure 4), which helps to reduce the negative impact of increased apparent porosity on the compressive strength of $MgAl_2O_4$ porous ceramic. In turn, during the sintering stage, $MgAl_2O_4$ grains will rearrange, and pores between particles will merge and grow. This phenomenon is conducive to improving the pore size (Figure 6) and ultimately enhancing the gas permeability of $MgAl_2O_4$ porous ceramic (Figure 10).

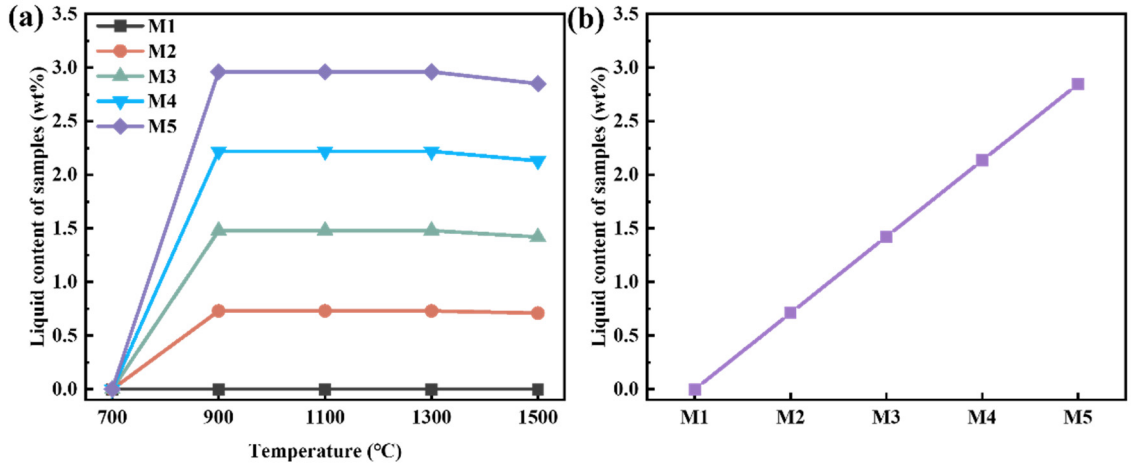

Figure 13. (**a**) Liquid contents of samples with different EDTA-$MgNa_2$ at different temperatures; (**b**) linear relationship between liquid content of samples and EDTA-$MgNa_2$ content at 1500 °C.

When compared to various porous ceramic filters (Figure 14 and Table 2), the $MgAl_2O_4$ porous ceramic filters developed in this work exhibit an outstanding overall balance of gas permeability and compressive strength. Notably, the compressive strength reaches 10.93 MPa, the highest among all compared samples, indicating superior structural integrity and resistance to mechanical stress, which are critical in harsh, high-temperature filtration environments. In addition, the material shows a gas permeability coefficient of 8.84 × 10^{-9} m^2, surpassing many porous ceramic filters. Overall, this finding facilitates further optimization of the gas permeance in high-temperature flue gas filters.

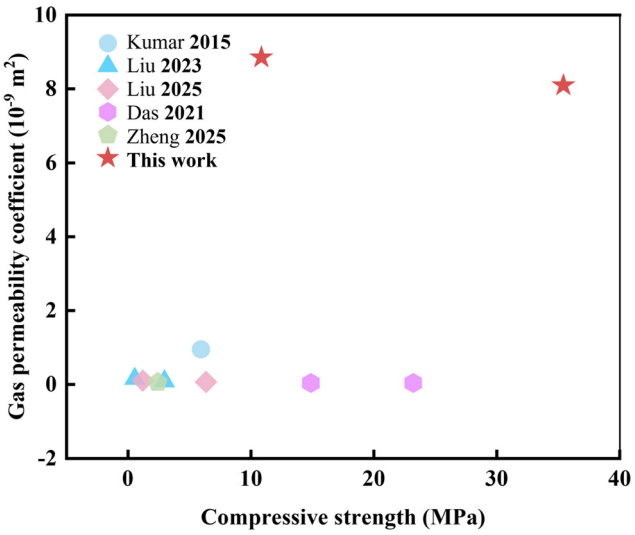

Figure 14. The compressive strength and gas permeability coefficient of different porous ceramics [11,13,19,31,32].

Table 2. Comparison of relevant data in different literature.

Porosity (%)	Compressive Strength (MPa)	Permeability (m^2)	Refs.
70.00	6.00	9.15×10^{-10}	[11]
56.04	3.03	4.73×10^{-11}	[13]
55.95	6.42	2.79×10^{-11}	[19]
39.89	14.97	2.20×10^{-12}	[31]
60.30	2.48	1.70×10^{-11}	[32]
56.28	10.93	8.84×10^{-9}	This work

5. Conclusions

To enhance the gas permeability and achieve high compressive strength of $MgAl_2O_4$ porous ceramics, EDTA-$MgNa_2$ was introduced as a pore former and sintering aid by the *in-situ* decomposition method. The effect of the content of EDTA-$MgNa_2$ on the gas permeability and performance of ceramics was investigated. The conclusions reached are as follows.

(1) The $MgAl_2O_4$ porous ceramic filters of 0–10 wt% exhibit a pressure drop of 0.84–3.72 hPa, gas permeability coefficient of 8.04×10^{-9}–8.84×10^{-9} m^2, gas permeability of 1.38–1.52 $mol \cdot m^{-2} \cdot s^{-1} \cdot Pa^{-1}$, compressive strength of 35.56–10.93 MPa, and apparent porosity of 47.27–56.28%.
(2) Increasing the EDTA-$MgNa_2$ content generates more pores in the sample, thereby increasing porosity and, consequently, enhancing the gas permeability coefficient. Meanwhile, the formation of neck bonds between particles mitigates the decrease in compressive strength caused by increased porosity.
(3) Simultaneously, the increase of open porosity is able to improve the pore connectivity, making the gas permeability of $MgAl_2O_4$ porous ceramics higher (8.04×10^{-9}–8.84×10^{-9} m^2).
(4) The optimal product is the ceramics prepared with 10 wt% EDTA-$MgNa_2$, which has a high gas permeability coefficient of 8.84×10^{-9} m^2, a compressive strength of 10.93 MPa, and a high apparent porosity of 56.28%.

Acknowledgments

The authors gratefully acknowledge the financial support provided by the Taishan Scholar Program of Shandong Province, Shandong Postdoctoral Science Foundation, Leader of Scientific Research Studio Program of Jinan, University of Jinan Disciplinary Cross-Convergence Construction Projects 2023, the Natural Science Foundation of Shandong Province, the Jinan City-School Integration Development Strategy Project, and the Shandong Provincial Key Research and Development Program.

Author Contributions

Methodology, J.L.; Investigation, J.L.; Writing—Original Draft Preparation, J.L.; Data Curation, J.L., C.Z.; Writing—Review & Editing, W.Z., Z.Z.; Supervision, L.Z., J.K., X.J.; Project Administration, W.Z.; Funding Acquisition, D.Z.

Ethics Statement

Not applicable.

Informed Consent Statement

Not applicable.

Data Availability Statement

The data are available from the corresponding author on reasonable request.

Funding

This research was funded by the Taishan Scholar Program of Shandong Province (No. tsqn202306225), Shandong Postdoctoral Science Foundation (No. SDBX2023025), Leader of Scientific Research Studio Program of Jinan (No. 2021GXRC082), University of Jinan Disciplinary Cross-Convergence Construction Projects 2023 (Nos. XKJC-202301 and XKJC-202311), the Natural Science Foundation of Shandong Province (Nos. ZR2024QE044 and ZR2025QC605), the Jinan City-School Integration Development

Strategy Project (Nos. JNSX2023015 and JNSX2023018), and the Shandong Provincial Key Research and Development Program (2025CXGC020107).

Declaration of Competing Interest

The authors declare that they have no known competing financial interests or personal relationships that could have appeared to influence the work reported in this paper.

References

1. Asadi M, Larki I, Forootan MM, Ahmadi R, Farajollahi M. Long-Term Scenario Analysis of Electricity Supply and Demand in Iran: Time Series Analysis, Renewable Electricity Development, Energy Efficiency and Conservation. *Sustainability* **2023**, *15*, 4618. DOI:10.3390/su15054618
2. Lee YY, Li IC, Kogularasu S, Huang BW, Wang YF, Masimukku S, et al. Advanced oxide-stabilized zirconia ceramics for flue gas filtration in air purification systems. *J. Hazard. Mater. Adv.* **2025**, *17*, 100539. DOI:10.1016/j.hazadv.2024.100539
3. Li P, Lin ZG, Du HB, Feng T, Zuo J. Do environmental taxes reduce air pollution? Evidence from fossil-fuel power plants in China. *J. Environ. Manag.* **2021**, *295*, 113112. DOI:10.1016/j.jenvman.2021.113112
4. Nacken M, Ma L, Heidenreich S, Verpoort F, Baron GV. Development of a catalytic ceramic foam for efficient tar reforming of a catalytic filter for hot gas cleaning of biomass-derived syngas. *Appl. Catal. B Environ.* **2012**, *125*, 111–119. DOI:10.1016/j.apcatb.2012.05.027
5. Chen YS, Hsiau SS, Syu JR, Chang YL. Clean coal technology on hot gas clean-up process with a moving granular bed filter. *Fuel* **2019**, *248*, 136–142. DOI:10.1016/j.fuel.2019.03.071
6. Park JH, Ahn JW, Kim KH, Son YS. Historic and futuristic review of electron beam technology for the treatment of SO_2 and NO_x in flue gas. *Chem. Eng. J.* **2019**, *355*, 351–366. DOI:10.1016/j.cej.2018.08.103
7. Chen Y, Yu C, Cheng X, Wang R, Deng C, Ding J, et al. Advances in Sintering Technologies for SiC Ceramics: Mechanisms, Challenges, and Industrial Applications. *High-Temp. Mater.* **2025**, *2*, 10013. DOI:10.70322/htm.2025.10013
8. Gu QL, Ng TCA, Bao YP, Ng HY, Tan SC, Wang J. Developing better ceramic membranes for water and wastewater Treatment: Where microstructure integrates with chemistry and functionalities. *Chem. Eng. J.* **2022**, *428*, 130456. DOI:10.1016/j.cej.2021.130456
9. Henning LM, Abdullayev A, Vakifahmetoglu C, Simon U, Bensalah H, Gurlo A, et al. Review on Polymeric, Inorganic, and Composite Materials for Air Filters: From Processing to Properties. *Adv. Energy Sustain. Res.* **2021**, *2*, 2100005. DOI:10.1002/aesr.202100005
10. Jia C, Liu YB, Li L, Song JN, Wang HY, Liu ZL, et al. A Foldable All-Ceramic Air Filter Paper with High Efficiency and High-Temperature Resistance. *Nano Lett.* **2020**, *20*, 4993–5000. DOI:10.1021/acs.nanolett.0c01107
11. Kumar A, Mohanta K, Kumar D, Parkash O. Low cost porous alumina with tailored gas permeability and mechanical properties prepared using rice husk and sucrose for filter applications. *Microporous Mesoporous Mater.* **2015**, *213*, 48–58. DOI:10.1016/j.micromeso.2015.04.004
12. Xiao CF, Han B. Preparation of porous silicon nitride ceramics by freeze drying. *J. Mater. Res. Technol.* **2019**, *8*, 6202–6208. DOI:10.1016/j.jmrt.2019.10.014
13. Liu ZL, Yuan L, Tian C, Peng ZJ, Zhang DY, Wen TP, et al. High gas permeability and directional channels of mullite porous ceramics prepared by pectin-based freeze-drying method. *Int. J. Appl. Ceram. Technol.* **2023**, *20*, 3552–3564. DOI:10.1111/ijac.14446
14. Zhou Y, Ye DC, Wu YQ, Zhang CX, Bai W, Tian YM, et al. Low-cost preparation and characterization of $MgAl_2O_4$ ceramics. *Ceram. Int.* **2022**, *48*, 7316–7319. DOI:10.1016/j.ceramint.2021.11.196
15. Wang F, Ye JK, He G, Liu GH, Xie ZP, Li JT. Preparation and characterization of porous $MgAl_2O_4$ spinel ceramic supports from bauxite and magnesite. *Ceram. Int.* **2015**, *41*, 7374–7380. DOI:10.1016/j.ceramint.2015.02.044
16. Deng WX, Yu XH, Sahimi M, Tsotsis TT. Highly permeable porous silicon carbide support tubes for the preparation of nanoporous inorganic membranes. *J. Membr. Sci.* **2014**, *451*, 192–204. DOI:10.1016/j.memsci.2013.09.059
17. Han F, Zhong ZX, Yang Y, Wei W, Zhang F, Xing WH, et al. High gas permeability of SiC porous ceramics reinforced by mullite fibers. *J. Eur. Ceram. Soc.* **2016**, *36*, 3909–3917. DOI:10.1016/j.jeurceramsoc.2016.06.048
18. Xing ZH, Hu YH, Xiang DP, Ma YP. Porous SiC-mullite ceramics with high flexural strength and gas permeability prepared from photovoltaic silicon waste. *Ceram. Int.* **2020**, *46*, 1236–1242. DOI:10.1016/j.ceramint.2019.09.052

19. Liu ZL, Gao J, Tian C, Zhang DY, Peng ZJ, Zhang LH, et al. Preparation and study of mullite ceramic fibre porous membranes with near-net shape forming and high gas permeability. *Ceram. Int.* **2025**, *51*, 2626–2638. DOI:10.1016/j.ceramint.2024.11.246
20. Esteban M, Vizcaíno MCP, Vílchez FG. The thermal behaviour of ethylenediaminetetracetic acid and its sodium salts. *Thermochim. Acta* **1983**, *62*, 257–265. DOI:10.1016/0040-6031(83)85045-X
21. II WPW, Stubican VS. Interdiffusion in the System MgO-$MgAl_2O_4$. *J. Am. Ceram. Soc.* **1971**, *54*, 349–352, DOI:10.1111/j.1151-2916.1971.tb12312.x
22. Li CW, Han Y, Wu LH, Chen K, An LN. Fabrication and properties of porous anorthite ceramics with modelling pore structure. *Mater. Lett.* **2017**, *190*, 95–98. DOI:10.1016/j.matlet.2016.12.131
23. Wu LH, Li CW, Chen YF, Wang CA. Seed assisted *in-situ* synthesis of porous anorthite/mullite whisker ceramics by foam-freeze casting. *Ceram. Int.* **2021**, *47*, 11193–11201. DOI:10.1016/j.ceramint.2020.12.244
24. Ma GS, Xia L, Zhang T, Zhong B, Yang H, Xiong L, et al. Permeability and thermal expansion properties of porous LAS ceramic prepared by gel-casting method. *J. Eur. Ceram. Soc.* **2020**, *40*, 3462–3468. DOI:10.1016/j.jeurceramsoc.2020.03.056
25. Roy S. Thermal properties of porous ceramics. *Open Ceram.* **2025**, *24*, 100867, DOI:10.1016/j.oceram.2025.100867
26. Nacken M, Heidenreich S, Hackel M, Schaub G. Catalytic activation of ceramic filter elements for combined particle separation, NO_x removal and VOC total oxidation. *Appl. Catal. B Environ.* **2007**, *70*, 370–376. DOI:10.1016/j.apcatb.2006.02.030
27. Xu XH, Liu X, Wu JF, Zhang C, Tian KZ, Yu JQ. Effect of preparation conditions on gas permeability parameters of porous SiC ceramics. *J. Eur. Ceram. Soc.* **2021**, *41*, 3252–3263. DOI:10.1016/j.jeurceramsoc.2021.01.015
28. Carter RE. Mechanism of Solid-state Reaction Between Magnesium Oxide and Aluminum Oxide and Between Magnesium Oxide and Ferric Oxide. *J. Am. Ceram. Soc.* **1961**, *44*, 116–120. DOI:10.1111/j.1151-2916.1961.tb13724.x
29. Yan JJ, Yan W, Chen Z, Nath M, Liao N, Li GQ, et al. A strategy for controlling microstructure and mechanical properties of microporous spinel ($MgAl_2O_4$) aggregates from magnesite and $Al(OH)_3$. *J. Alloys Compd.* **2022**, *896*, 163088. DOI:10.1016/j.jallcom.2021.163088
30. Salomão R, Arruda CC, Pandolfelli VC, Fernandes L. Designing high-temperature thermal insulators based on densification-resistant *in situ* porous spinel. *J. Eur. Ceram. Soc.* **2021**, *41*, 2923–2937. DOI:10.1016/j.jeurceramsoc.2020.12.014
31. Das D, Kayal N. Permeability and dust filtration behaviour of porous SiC ceramic candle filter. *Mater. Today Proc.* **2021**, *39*, 1235–1240. DOI:10.1016/j.matpr.2020.04.090
32. Zheng DZ, Hu YW, Liang SO, Wang ZM. Enhancing high-temperature gas filtration performance of mullite fiber-based porous ceramics by optimizing the fiber-to-colloid ratio. *J. Alloys Compd.* **2025**, *1036*, 181632. DOI:10.1016/j.jallcom.2025.181632